ACS APPLIED MATERIALS & INTERFACES

Research Article

Modulating Lipoprotein Transcellular Transport and Atherosclerotic Plaque Formation in ApoE$^{-/-}$ Mice via Nanoformulated Lipid−Methotrexate Conjugates

Valentina Di Francesco, Danila Gurgone, Roberto Palomba, Miguel Filipe Moreira Marques Ferreira, Tiziano Catelani, Antonio Cervadoro, Pasquale Maffia,[¶] and Paolo Decuzzi*,[¶]

Cite This: *ACS Appl. Mater. Interfaces* 2020, 12, 37943−37956

Read Online

ACCESS | Metrics & More | Article Recommendations | SI Supporting Information

ABSTRACT: Macrophage inflammation and maturation into foam cells, following the engulfment of oxidized low-density lipoproteins (oxLDL), are major hallmarks in the onset and progression of atherosclerosis. Yet, chronic treatments with anti-inflammatory agents, such as methotrexate (MTX), failed to modulate disease progression, possibly for the limited drug bioavailability and plaque deposition. Here, MTX−lipid conjugates, based on 1,2-distearoyl-*sn*-glycero-3-phosphoethanolamine (DSPE), were integrated in the structure of spherical polymeric nanoparticles (MTX-SPNs) or intercalated in the lipid bilayer of liposomes (MTX-LIP). Although, both nanoparticles were colloidally stable with an average diameter of ∼200 nm, MTX-LIP exhibited a higher encapsulation efficiency (>70%) and slower release rate (∼50% at 10 h) compared to MTX-SPN. In primary bone marrow derived macrophages (BMDMs), MTX-LIP modulated the transcellular transport of oxLDL more efficiently than free MTX mostly by inducing a 2-fold overexpression of ABCA1 (regulating oxLDL efflux), while the effect on CD36 and SRA-1 (regulating oxLDL influx) was minimal. Furthermore, in BMDMs, MTX-LIP showed a stronger anti-inflammatory activity than free MTX, reducing the expression of IL-1β by 3-fold, IL-6 by 2-fold, and also moderately of TNF-α. In 28 days high-fat-diet-fed apoE$^{-/-}$ mice, MTX-LIP reduced the mean plaque area by 2-fold and the hematic amounts of RANTES by half as compared to free MTX. These results would suggest that the nanoenhanced delivery to vascular plaques of the anti-inflammatory DSPE-MTX conjugate could effectively modulate the disease progression by halting monocytes' maturation and recruitment already at the onset of atherosclerosis.

KEYWORDS: *nanomedicine, atherosclerosis, foam cells, inflammation, low-density lipoprotein transport*
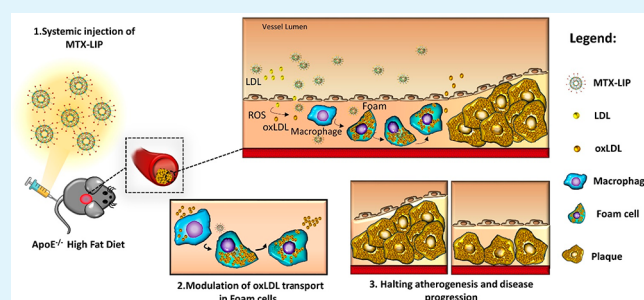
INTRODUCTION

Atherosclerosis is an inflammatory disorder affecting large and medium size arteries and is responsible for acute cardiovascular syndromes, such as myocardial infarction (MI) and stroke.[1] Immune cells play a key role in all the stages of the pathology, from endothelial dysfunction to plaque formation and rupture.[2] Atherosclerotic vascular lesions are established by the continuous infiltration of circulating monocytes into the arterial walls and their progressive maturation into macrophages and foam cells.[3] These are lipid-rich macrophages that have uptaken large amounts of oxidized low-density lipoproteins (oxLDLs), mostly through specific surface receptors such as CD36 and SRA-1.[4] Therefore, one strategy to prevent atherosclerotic plaque formation and progression relies on reducing vascular inflammation.[5,6]

Recently, methotrexate (MTX), which is a potent chemotherapeutic and anti-inflammatory agent, was proposed for the treatment of atherosclerosis in patients affected by chronic inflammatory diseases, such as rheumatoid arthritis and psoriatic arthritis. MTX is known to possess anti-inflammatory properties and is capable of lowering the production of pro-inflammatory cytokines by macrophages.[7] MTX has been shown to increase cellular levels of adenosine monophosphate and adenosine, which consequently suppress the secretion of cytokines by immune cells and may protect against ischemic injury.[8] In particular, upregulation of the adenosine receptor limits the formation of foam cells by promoting lipoprotein efflux out of macrophages.[9] Despite all these properties, in the cardiovascular inflammation reduction trial (CIRT), a low-dose MTX treatment failed to lower secondary cardiovascular event rates.[10] It is important, however, to note that the free molecule
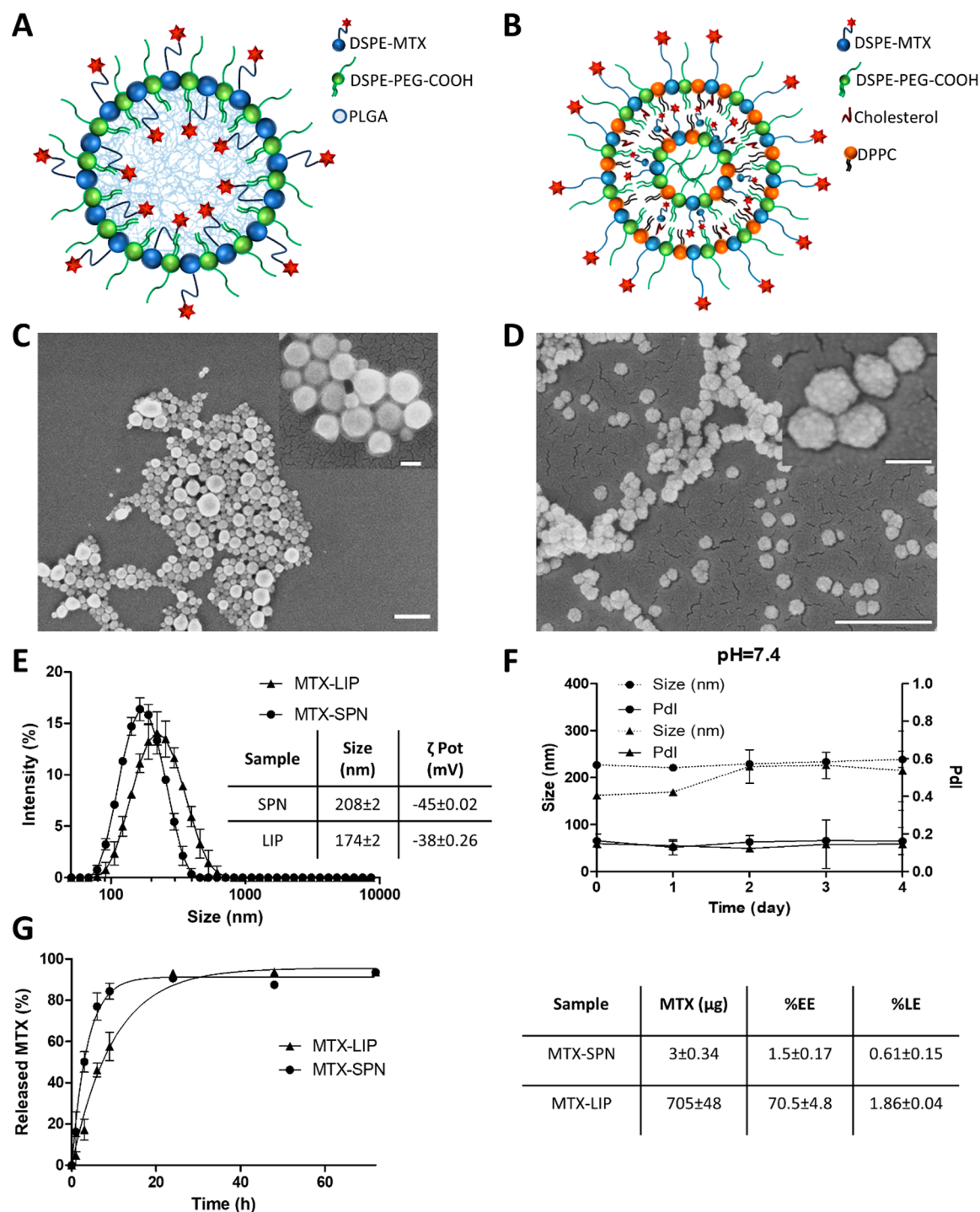
37943
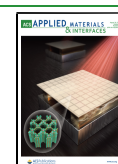
Figure 1. Physicochemical and pharmacological characterization of MTX-loaded nanoparticles. (A, B) Schematic representation of MTX-SPN and MTX-LIP, respectively. (C, D) Scanning electron microscopy images of SPN and LIP, respectively (scale bar: 500 nm; up-right inset scale bar: 100 nm). (E, F) Hydrodynamic diameter and colloidal stability of MTX-SPN and MTX-LIP via dynamic light-scattering analysis. (G) Release studies for MTX from MTX-SPN and MTX-LIP. The table summarizes the absolute drug mass, encapsulation efficiency (%EE), and loading (%LE) data for MTX into MTX-SPN and MTX-LIP.

MTX is hydrophobic, suffers low solubility in physiological environments, has a modest half-life in blood, and can induce severe adverse effects, including myelosuppression, neutropenia, infections, thrombocytopenia, and bone marrow suppression.[11,12]

MTX reformulation into nanoparticles could help to overcome the above-mentioned limitations, thus harnessing the full potential of this drug. Indeed, many groups have investigated the benefits associated with the encapsulation of MTX into liposomes, specifically focusing their attention on the pharmacokinetic parameters. For instance, Chen and co-workers showed that the plasma concentration of MTX drops rapidly upon intravenous administration, being nearly undetectable after only 4 h.[12] Conversely, MTX-loaded liposomes provided an over 5-fold increase in circulation half-life and mean residence time and a 16-fold increase in the area under the

concentration−time curve (AUC 0−24), as compared to the free molecule.[12] Similar results were also reported by Alekseeva et al., documenting a 4-fold improvement in drug bioavailability for the MTX−liposomes over the free drug.[13] Also, a few studies have started to show that the atheroprotective properties of MTX can be more effectively exploited by administering nanoparticles loaded with the drug rather than the free molecule.[14,15] For instance, MTX-loaded polymeric nanoparticles were shown by the authors to mitigate atherosclerotic progression in apolipoprotein-E (apoE)$^{-/-}$ mice, fed with a high-fat diet (HFD).[16] Indeed, accumulation of blood-borne nanoparticles into atherosclerotic plaques would increase the dose of MTX delivered specifically to the inflamed arterial wall, avoiding side effects associated with systemic exposure. Nanoparticle accumulation is supported by different and multiple mechanisms, including the direct nanoparticle uptake by phagocytic macrophages;[17−19] the deposition within the diseased tissue due to favorable, local hydrodynamic conditions (recirculation area and low wall shear stresses), hyper-permeability of a dysfunctional endothelium and increased angiogenesis;[20−24] the direct plaque localization via molecular targeting;[25−28] and the nanoparticle uptake by circulating monocytes that would eventually infiltrate the plaque.[29,30]

In this work, two different types of nanoparticles—polymeric- and lipid-based nanoparticles—were designed, realized, and tested *in vitro* and *in vivo* for the delivery of MTX. Different from previous works, these nanoparticles were realized using a lipid−MTX conjugate, obtained by reacting MTX with the lipid chain 1,2-distearoyl-*sn*-glycero-3-phosphoethanolamine (DSPE). These lipid−MTX conjugates would enhance nanoparticle loading and facilitate the intracellular delivery of the anti-inflammatory molecule. For the polymeric nanoparticles, the DSPE−MTX conjugate was dispersed as a regular payload within the hydrophobic core, whereas for the liposomes, the DSPE-MTX was integrated in the lipid bilayer, thus providing both a therapeutic and a structural function. After extensive biophysical and pharmacological characterizations, MTX-loaded spherical polymeric nanoparticles (MTX-SPNs) and MTX-loaded liposomes (MTX-LIPs) were tested *in vitro* to demonstrate their ability to modulate oxLDL uptake by macrophages and *in vivo* to assess the atheroprotective efficacy in hyperlipidemic mice.

■ RESULTS

Physicochemical and Pharmacological Characterization of MTX-Loaded Nanoparticles. Methotrexate (MTX) is a potent anti-inflammatory molecule with a low solubility in physiological fluids[31] and a modest half-life in blood.[32] The formulation of MTX into nanoparticles can overcome the limitations above, thus harnessing the full potential of this drug. Two different nanotechnological platforms—spherical polymeric nanoparticles (SPNs) and liposomes (LIPs)—were considered for the systemic delivery of methotrexate. The MTX-SPNs were realized via a single emulsion technique, resulting in a PLGA hydrophobic core that is externally stabilized by a lipid monolayer, including carboxyl-terminated DSPE-PEG molecules (Figure 1A). The MTX-LIPs were realized via a thin-layer evaporation method (TLE) using DPPC, cholesterol, and carboxyl-terminated DSPE-PEG chains (Figure 1B). The anti-inflammatory molecule MTX was included in the structure of the two nanoparticles in the form of a DSPE-MTX conjugate (Figure S1). This was generated by reacting 1,2-distearoyl-*sn*-glycero-3-phosphoethanolamine-*N*-amino (DSPE-NH$_2$) with a DCC/NHS preactivated MTX. The resulting DSPE-MTX conjugate is highly lipophilic and was included within the hydrophobic PLGA core and surface-stabilizing lipid layer of SPN, and for the LIP, it was integrated naturally in the double lipid layer.

Scanning electron microscopy images of MTX-SPN and MTX-LIP are provided in Figure 1C and 1D, respectively. The top right insets provide magnified views of the same nanoparticles. The electron microscopy analysis demonstrates the sphericity and uniform size distribution of both MTX-loaded nanoparticles, exhibiting a diameter in the neighborhood of 200 nm. More precisely, a dynamic light scattering analysis returned an average hydrodynamic diameter of 208 ± 2 nm and 174 ± 2 nm for the MTX-SPN and MTX-LIP, respectively (Figure 1E). Both nanoparticle formulations were characterized by a moderate polydispersity index (PDI) $\sim$ 0.15, in agreement with the electron microscopy observations. Given the presence of carboxyl-terminated DSPE-PEG chains, both nanoformulations presented a negative surface electrostatic ζ potential of -45 ± 0.02 mV for the MTX-SPN and -38 ± 0.26 mV for the MTX-LIP. These values are also listed in the table included in Figure 1E. For both nanoformulations, colloidal stability tests were performed under physiological conditions at pH = 7.4 and in a slightly acidic environment with a pH = 6.5. The average hydrodynamic diameters and PDI of both nanoparticles were monitored up to 4 days. Under physiological conditions, the data in Figure 1F show very stable formulations with a percentage change in size and PDI lower than 10% through the entire observation period. Differently, at pH = 6.5, the data in Figure S2 present a steadily growing size for both MTX-LIP and MTX-SPN most likely resulting from the progressive rearrangement of the colloidal solution. Overall, however, the MTX-LIP resulted to be more stable than the MTX-SPN. It is here important to recall that the conjugate in the MTX-LIP provides also a structural contribution in addition to the pharmacological function in that it is directly included in the double-lipid layer of the liposomes.

Next, high performance liquid chromatography (HPLC) was employed to measure the loaded and released amounts of MTX from the two nanoformulations. MTX encapsulation efficiency EE was evaluated as the percentage ratio between the actual loaded mass of the drug and the input mass of the drug during nanoparticle realization. For the MTX-LIP, a significantly high EE was measured to be equal to $70.5 \pm 4.8\%$, whereas this value dropped to only $1.5 \pm 0.7\%$ for the MTX-SPN, with a total mass of the loaded DSPE-MTX, corresponding to 705 ± 48 and 3 ± 0.34 μg per single nanoparticle preparation, respectively. The MTX loading was $1.86 \pm 0.04\%$ for LIP and $0.61 \pm 0.15\%$ for SPN. The modest drug loading associated with the SPN is in line with previous data from the authors on other hydrophobic drug molecules.[33] Note that, in the MTX-LIP, the DSPE-MTX conjugate can intercalate with the DPPC and DPSE-PEG chains in forming the liposome double-lipid membrane. This increases significantly the amounts of drug that can be incorporated into the particles. The release profiles for MTX from SPN and LIP were determined in a 4 L PBS solution (infinite sink condition) and are plotted in Figure 1G. MTX was more rapidly released from the SPN as compared to the LIP. At 9 h post study initiation, over 80% of the drug was released out of the SPN, whereas about 50% came out of the MTX-LIP. After 1 day, almost 90% of the encapsulated MTX was released from both nanoparticles. At later time points, the release profiles reached a plateau close to 100%. Indeed, the higher stability of MTX-LIP

over MTX-SPN is also shown by the overall lower MTX release rates associated with the former particles.

It is here important to note that the EE = 1.5 ± 0.7% for the SPN results from an extensive and systematic optimization process that led to define 12 different MTX-loaded SPN formulations with the final objective of improving drug loading in these particles. From the data listed in Figure S3, the following parameters were changed in the synthesis of SPN: total mass of PLGA, ranging from 0.5 to 2 mg; molecular weight of PLGA, varying from low (23−35 kDa) to high (38−53 kDa); and the ratios between DPPC, DSPE-PEG, and DSPE-MTX. The resulting encapsulation efficiency varied from a minimum of 0.13% to a maximum of 1.5%. In the rest of the manuscript, MTX-SPNs are referred to as realized with 2 mg of high molecular weight PLGA, no DPPC, 0.2 mg of DSPE-MTX, and 0.11 mg of DSPE-PEG.

Macrophage Maturation to Foam Cells and Nanoparticle Uptake. Foam cells were obtained by feeding macrophages with oxidized low-density lipoproteins (oxLDL). The continuous accumulation of these ∼20 nm oxidized lipid particles (see TEM images in Figure S4) into macrophages is responsible for their maturation into foam cells, which is a fundamental step in the progression of atherosclerotic plaques. LDL oxidation was performed using copper salts ($CuSO_4$), and two different cell types were exposed to oxLDL, namely, the murine cell line Raw 264.7 and the primary bone marrow derived macrophages (BMDMs) isolated from the femur of rats. First, the dose-dependent engulfment of oxLDL molecules into phagocytic cells was assessed. To this end, Raw 264.7 were incubated overnight with different amounts of oxLDL, namely, 0, 20, 50, and 80 μg/mL, and then stained with Oil Red O (ORO). In Figure S5, the fluorescent intensity associated with the ORO staining is shown to grow proportionally with the initial amount of oxLDL. An intermediate concentration of 50 μg/mL of oxLDL was considered as appropriate for all foam cell experiments. Then, the precise intracellular localization of oxLDL molecules was assessed via correlative light and electron microscopy (CLEM).[34] This technique allowed the authors to coregister together data from fluorescent confocal microscopy and transmission electron microscopy. For the fluorescent microscopy experiments, the DiI dye was stably adsorbed onto oxLDL (Figure S6 and Supporting Videos), while macrophages were treated with 488-lysotracker and DAPI to highlight the lysosomes and nuclei, respectively. Figure 2A shows a transmission electron micrograph (left) and a confocal fluorescent image (center) of a representative foam cell, obtained by feeding RAW 264.7 cells overnight with 50 μg/mL of oxLDL. In the right inset of the same image, the TEM and confocal images were registered and combined together. These figures demonstrate a massive localization of oxLDL molecules (red) into lysosomes (green) around the nucleus (blue). Also, the TEM image shows the lysosomes as light structures due to the high lipid content and local density. Indeed, in TEM analyses of control cells (Figure S7), lysosomes appear significantly darker. This again would support the notion that oxLDL molecules are uptaken in a dose-dependent manner by phagocytic cells and tend to localize within the lysosomes.

In order to deliver their therapeutic cargo, MTX-loaded nanoparticles should cross the plasma membrane and be uptaken by the macrophages. Therefore, the time-dependent internalization of LIP and SPN into BMDM (i.e., before exposure to oxLDL) and foam cells (i.e., after exposure to oxLDL) was assessed via confocal fluorescent microscopy and
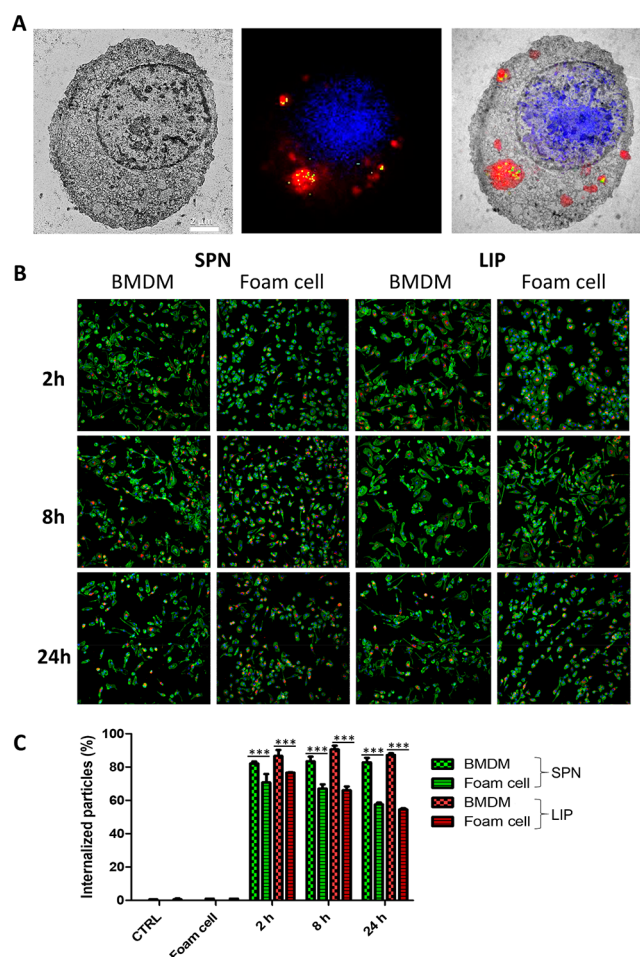

Figure 2. Macrophage maturation to foam cells and nanoparticle uptake. (A) Correlative light and electron microscopy (CLEM) characterization for macrophages exposed to oxidized low-density lipoprotein (oxLDL)—transmission electron microscopy image (left); confocal fluorescent microscopy image (center) showing the cell nucleus (blue, DAPI), the cell lysosomes (green, LysoTrackerGreen), and oxLDL molecules (red, Dil); light and electron microscopy images overlap (right) (scale bar: 2 μm). (B) Representative confocal images of BMDM and foam cells exposed to SPN (left) and LIP (right) at different time points (2, 8, and 24 h). (C) Flow cytometry analysis BMDM and foam cells exposed to SPN and LIP at different time points (2, 8, and 24 h). *** $p < 0.001$.

flow cytometry analysis. Figure 2B shows representative confocal fluorescent images of macrophages (BMDMs) and foam cells incubated with Cy5-labeled SPN (left) and Cy5-labeled LIP (right). Both nanoparticles (red dots) were readily internalized from the two cell types. However, a significant difference was detected in uptake propensity between the BMDM (no exposure to oxLDL) and foam cells. The latter tend to engulf a smaller number of nanoparticles. This was also confirmed and quantified via flow cytometry, with the data presented in Figure 2C for both LIP and SPN. The percentage of BMDM associated with nanoparticles (i.e., percentage of positive events) was quite constant over time for both LIP and SPN. Specifically, for the three tested time points (2, 8, and 24 h), this percentage was equal to 86.66 ± 3.59, 90.60 ± 2.23, and 87.30 ± 0.96 for LIP and 82.2 ± 1.1, 83.43 ± 2.82, and 82.87 ± 2.67 for SPN. In foam cells, for the three tested time points (2, 8, and 24 h), this same percentage was generally lower as compared to BMDM and equal to 76.7 ± 0.14, 66.1 ± 2.26, and 54.6 ± 0.71

for LIP and 70.8 ± 5, 67.1 ± 2.54, and 57.65 ± 1.06 for SPN. The difference in uptake propensity between foam cells and BMDM is more evident at the latest time point (24 h). This difference could be associated with the fact that the large amounts of oxLDL stored in the lysosomes of foam cells would affect the internalization capacity of the cell. Notice also, that in agreement with the above results, other authors have documented that macrophages fed with huge amounts of lipids tend to lose their phagocytic capacity.[35−37] It is just important to highlight that the Cy5-SPN and Cy5-LIP are comparable in size and surface properties to the parent MTX-SPN and MTX-LIP. Also, the conjugation of Cy5 molecules on the particle surface was shown to be very stable (Figure S8).

Role of Methotrexate in Macrophage Maturation to Foam Cells. As feeding macrophages with oxLDL is responsible for the progressive transition toward foam cells, a reduction of intracellular oxLDL would restore cell homeostasis and reverse the maturation process. Indeed, this could be achieved in two different ways: limit the uptake of oxLDL and foster the efflux of oxLDL. Importantly, MTX atheroprotection has been speculated to be associated with both its anti-inflammatory effect and ability to modulate cholesterol transport.[38] Therefore, in order to assess the effect of MTX on LDL trafficking, BMDMs were first treated overnight with 50 μg/mL of Dil-oxLDL to induce foam cell formation, and then the same cells were treated for 24 h with different interventions, namely, free MTX, empty LIP, MTX-LIP, empty SPN, and MTX-SPN. After 24 h, fluorescent images were acquired to quantify the amounts of intracellular DiI-oxLDL. Figure 3A shows representative microscopy pics for the untreated foam cells (control experiment), free MTX, and empty LIP-treated foam cells; MTX-LIP-treated foam cell; empty SPN-treated foam cells; MTX-SPN-treated foam cell; and the original BMDM, which were not exposed to oxLDL. These images clearly demonstrate the progressive decrease in fluorescent intensity associated with the cells as moving from the untreated foam cells (top) to the MTX-loaded nanoparticle-treated cells (bottom). The fluorescent intensity for the different interventions is also quantified in the bar chart of Figure 3B, where the data are normalized by the number of cells within the region of interest. No statistical significant difference was observed between the three control groups—untreated foam cells (0.39 ± 0.0004/cell); empty LIP-treated foam cells (0.46 ± 0.03/cell); empty SPN-treated foam cells (0.39 ± 0.03/cell); and free MTX-treated foam cells (0.36 ± 0.015/cell). On the other hand, the MTX-LIP and MTX-SPN are significantly more effective than the free drug in decreasing the amounts of intracellular lipids (0.09 ± 0.009/cell and 0.09 ± 0.026/cell, respectively, vs 0.36 ± 0.015/cell − p < 0.0001). This should be probably ascribed to the fact that the MTX-loaded nanoparticles are more efficiently uptaken by the cells as compared to the free drug molecules. In all fluorescent images, filamentous actin was stained to highlight the cell body (green signal), and nuclei were stained using DAPI (blue signal).

In addition to the fluorescent signal quantification, the intracellular total cholesterol amounts were also measured, following the same treatment conditions as per the confocal microscopy analysis above. However, in this case, two different time points were considered, namely, 8 and 24 h, for the intervention. Data are provided in Figure 3C and D for the LIP- and SPN-based treatments at 8 and 24 h, respectively. The intracellular total cholesterol analysis confirmed the trends observed via confocal fluorescent microscopy. The cholesterol content was observed to reduce as moving from untreated foam
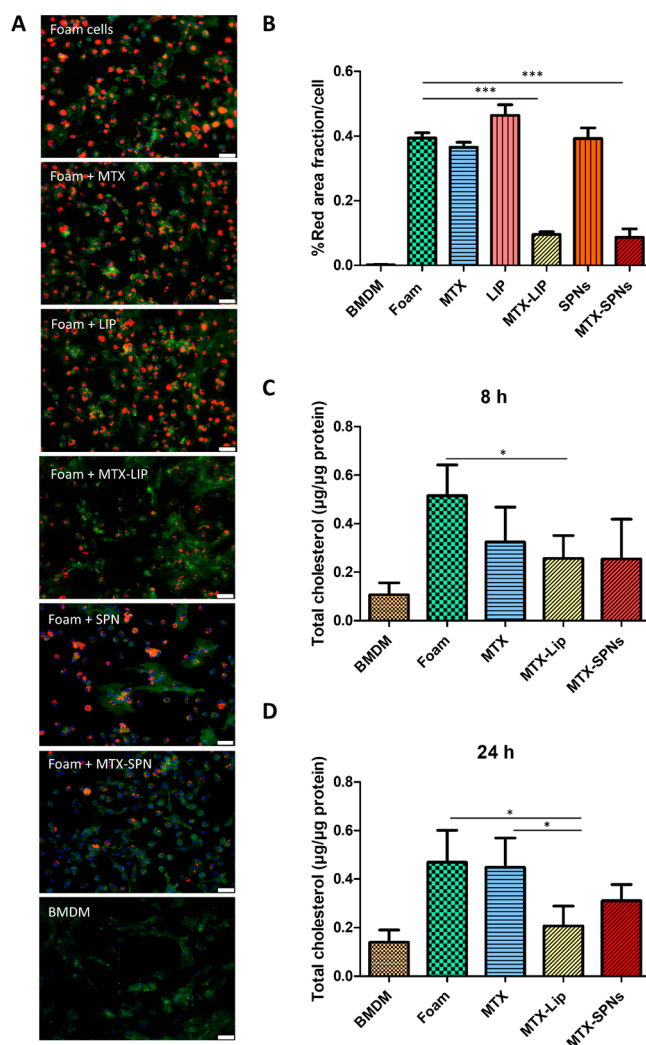

Figure 3. Role of methotrexate in macrophage maturation to foam cells. (A) Representative fluorescence images of different treatments conducted on BMDM forced to become foam cell following exposure to oxLDL (50 μg/mL). Red: Dil-oxLDL; blue: DAPI; green: F-Actin. From top to bottom, untreated foam cells, 24 h free MTX-treated foam cells, 24 h empty LIP-treated foam cells, 24 h MTX-LIP-treated foam cells; 24 h empty SPN-treated foam cells 24 h MTX-SPN-treated foam cells, and BMDM not exposed to oxLDL (scale bar: 50 μm). (B) Quantification of the oxLDL accumulation into cells expressed as the ratio between the size of the red area (Dil-oxLDL) and cell number. (Data are expressed as average ± SEM of n = 10 biological replicates. *** p < 0.0001.) (C, D) Quantification of the total cholesterol in macrophages treated with oxLDL (50 μg/mL) and exposed to MTX, MTX-LIP, or MTX-SPN for 8 and 24 h. (Data are reported as average ± SD of n = 4 biological replicates (* p < 0.01, *** p < 0.0001).

cells to free MTX-treated foam cells, MTX-LIP- and MTX-SPN-treated foam cells, and eventually the BMDM, both at 8 and 24 h. Larger differences between the control groups and the nanoparticle-treated foam cells were detected at 24 h as compared to the earlier 8 h time point. Notice that both MTX-LIP and MTX-SPN were able to decrease the intracellular cholesterol content at 8 h, returning values of 0.25 ± 0.09 μg/μg protein and 0.25 ± 0.16 μg/μg protein, respectively. At 24 h, the two formulations reduced the cholesterol amounts to 0.20 ± 0.08 μg/μg of protein and 0.31 ± 0.07 μg/μg of protein as compared to the untreated foam cells 0.44 ± 0.12 μg/μg of

A　　　8h

B　　　24h

C

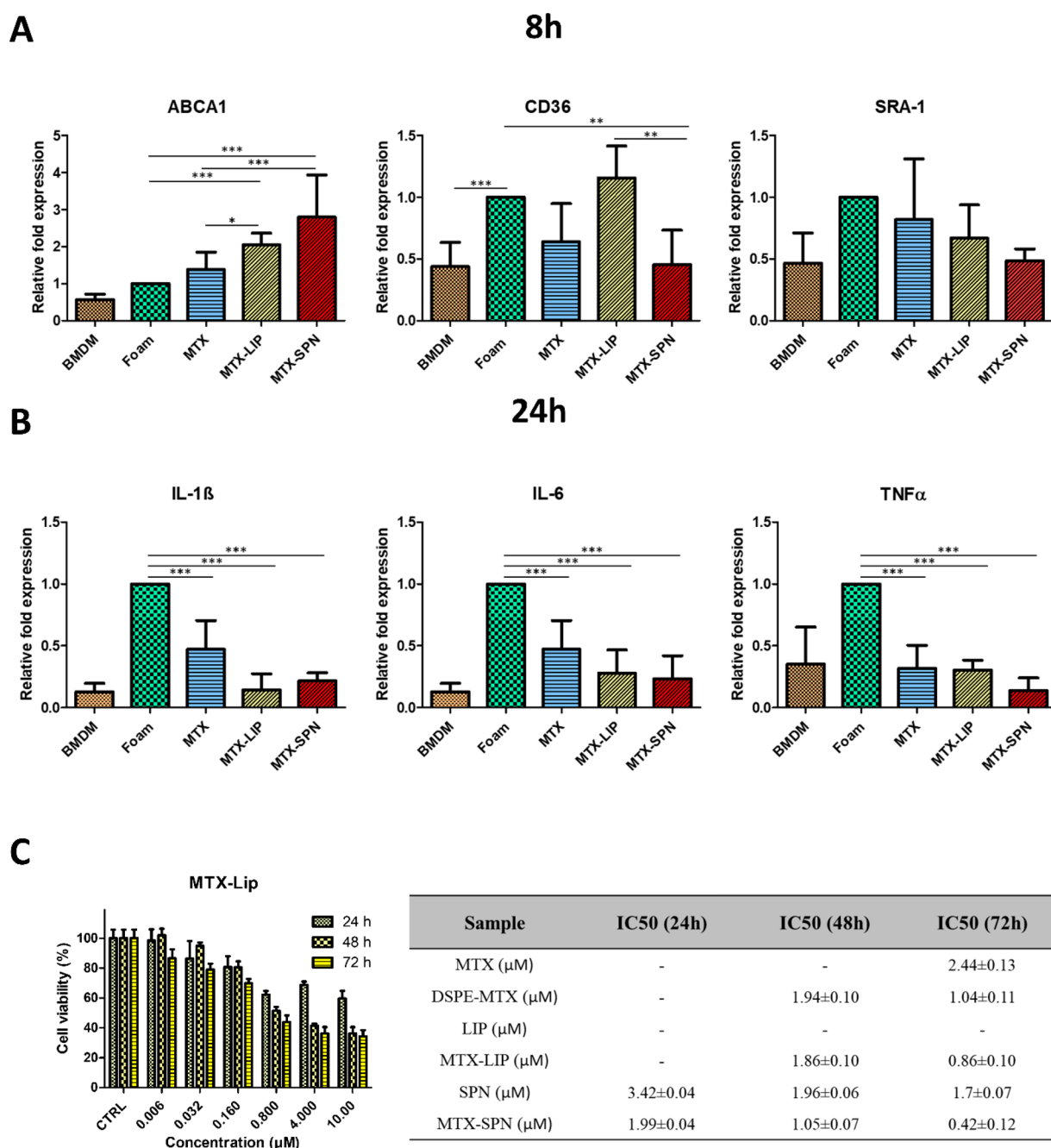| Sample	IC50 (24h)	IC50 (48h)	IC50 (72h)
MTX (μM)	-	-	2.44±0.13
DSPE–MTX (μM)	-	1.94±0.10	1.04±0.11
LIP (μM)	-	-	-
MTX-LIP (μM)	-	1.86±0.10	0.86±0.10
SPN (μM)	3.42±0.04	1.96±0.06	1.7±0.07
MTX-SPN (μM)	1.99±0.04	1.05±0.07	0.42±0.12

Figure 4. Expression of cholesterol transport and inflammatory genes in macrophages and cell viability. (A) Expression level of foam cells markers (ABCA1, CD36, and SRA-1) in macrophages treated with free MTX, MTX-LIP, and MTX-SPN for 8 h. (B) Expression level of pro-inflammatory cytokines (IL-1β, IL-6, and TNF-α) in macrophages treated with free MTX, MTX-LIP, and MTX-SPN for 24 h. (Data are expressed as average ± SD ($n = 5$); *** $p < 0.0001$; ** $p < 0.001$; * $p < 0.01$). (C) BMDM viability upon incubation with MTX-LIP (left). The table (right) summarizes the IC50 values on BMDM at 24, 48, and 72 h post exposure to different therapeutic groups, namely, free MTX, DSPE–MTX, empty LIP, MTX-LIP, empty SPN, and MTX-SPN.

protein. In general, MTX-LIP tended to be more effective than the MTX-SPN, especially at 24 h.

Modulating the Expression of Cholesterol Transport and Inflammatory Genes in MTX-Treated Foam Cells. The expression of three foam cell markers (ABCA1, CD36, and SRA-1) and three inflammatory genes (IL-1β, IL-6, and TNF-α) was measured by real-time PCR in response to different treatment conditions, namely, free MTX, empty LIP, empty SPN, MTX-LIP, and MTX-SPN. Untreated foam cells and BMDM (not exposed to oxLDL) were used as control groups. The foam cell marker ABCA1 is involved in cholesterol efflux,

whereas the markers CD36 and SRA-1 are known to regulate cholesterol influx. The overexpression of CD36 and SRA-1 is a landmark for the maturation of macrophages into foam cells. Specifically, it should be here recalled that CD36 recognizes the lipid moieties in the oxLDL molecules, while SRA-1 binds to the oxidized portion of the lipoprotein.[39] The gene expression analysis was performed at two different time points, namely, 8 and 24 h. Data are presented in Figure 4 and Figures S9 and S10, where the gene expression levels are normalized with respect to foam cells, which are arbitrarily taken as equal to 1. Importantly, a direct comparison between BMDM (not exposed to oxLDL)
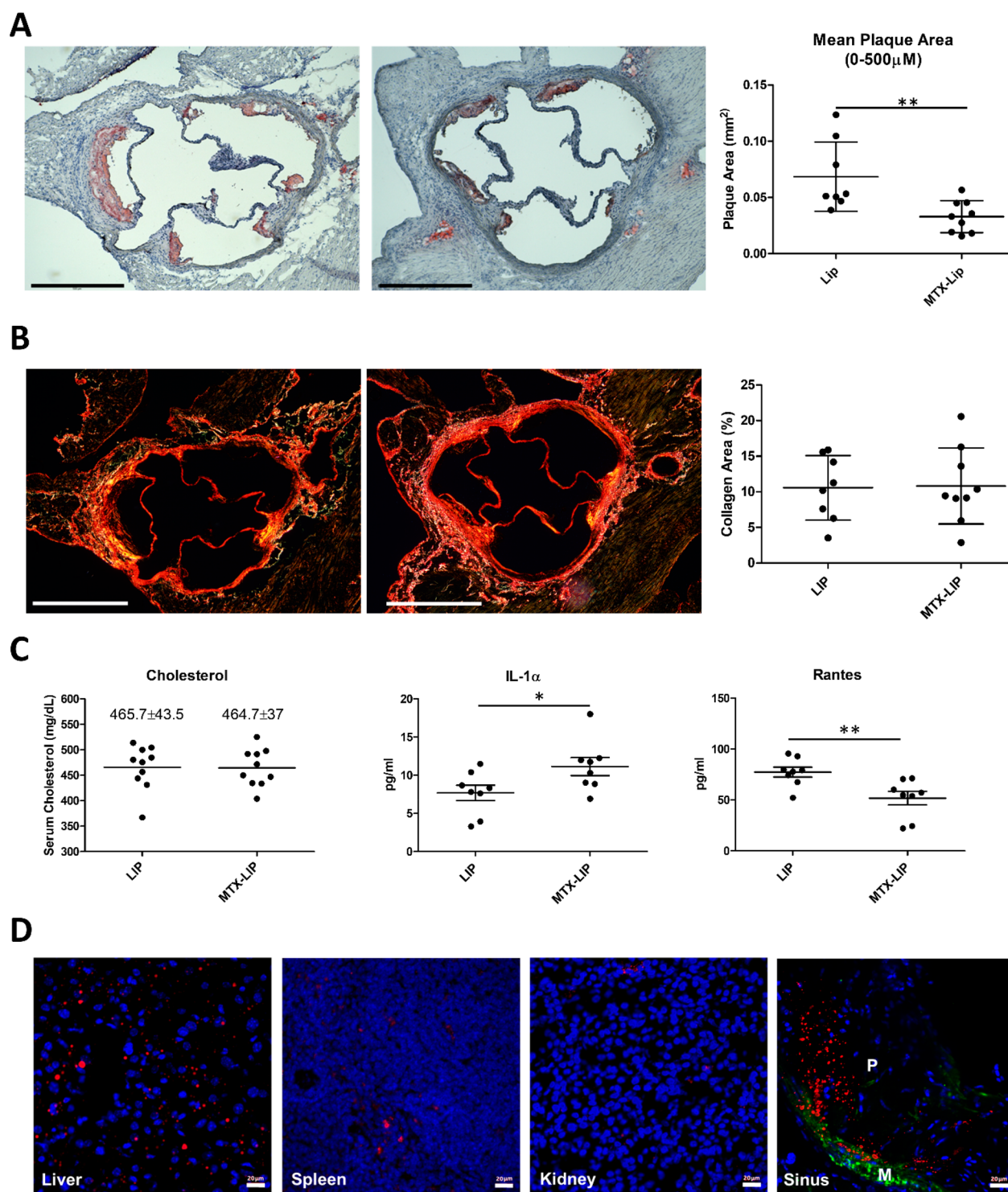
Figure 5. Preclinical characterization of MTX-liposomes. (A) Representative photomicrographs (left) of oil red O (ORO)-stained aortic sinuses (scale bar: 500 μm) and quantification of the mean lesion area (right) for empty LIP and MTX-LIP treatments. (B) Representative images of plaque collagen content (left) by picrosirius red staining (scale bar: 500 μm) and quantification of the collagen area (right) for empty LIP and MTX-LIP treatments. For plots in (A) and (B), individual data points represent average value per mouse; horizontal bars denote mean. **$p < 0.01$. (C) Analyses of cholesterol, IL-1α, and RANTES serum content for empty LIP and MTX-LIP treatments. Individual data points represent average value per mouse, and horizontal bars denote mean. Results are presented as mean $\pm$ SEM and analyzed by a Student unpaired t test. * $p < 0.05$, ** $p < 0.01$. (D) Cy5-LIP (red signal) biodistribution in liver, spleen, kidneys, and aortic sinus. Green: α-smooth muscle actin (α-SMA). Blue: cell nuclei. In the aortic sinus image: M indicates media and P indicates plaque (scale bar: 20 μm).

and foam cells reveals a 2 to 3 times increase in the expression of CD36 and SRA-1, at both 8 and 24 h. Indeed, this continues to demonstrate that an overnight exposure of BMDM to 50 μg/mL of oxLDL is sufficient to trigger the maturation into foam cells.

Figure 4A shows the expression of the three genes regulating the transport of cholesterol at 8 h. For ABCA1, the relative fold expression increase was equal to 1.383 ± 0.468 for free MTX; 2.048 ± 0.31 for MTX-LIP; and 2.793 ± 1.14 for MTX-SPN. Indeed, an increase in ABCA1 would be mirrored into an increase in cholesterol efflux. For CD36 and SRA-1, modest variations around a relative fold expression of 1 were observed for almost all treatments, implying that MTX has lower or no significant effect on these genes. Specifically, the relative fold expression induced by LIP-MTX was 1.156 ± 0.257 for CD36 and 0.668 ± 0.269 for SRA-1, and that induced by MTX-SPN was 0.454 ± 0.279 for CD36 and 0.485 ± 0.096 for SRA-1. These data would suggest that the treatment of foam cells with the nanoformulated MTX would induce a significant over-expression of ABCA1, thus boosting cholesterol efflux, and a moderate downregulation of CD36, which is involved in cholesterol influx. At 24 h, on the other hand, a strong reduction in the expression of all three genes was recorded for the MTX-SPN (Figure S9), whereas for the MTX-LIP a significant reduction was observed only for the SRA-1.

As per the inflammatory response, an overall decrease of all three genes was observed at both 8 and 24 h upon treating the foam cells with either free MTX or MTX-loaded nanoparticles (Figure S10). However, the anti-inflammatory effect appears more clearly after 24 h (Figure 4B).

For IL-1β, the relative fold expression was reduced to 0.143 ± 0.129 for the MTX-LIP and to 0.215 ± 0.065 for the MTX-SPN, which are both comparable with the level of relative expression measured in BMDM (0.127 ± 0.067). Free MTX treatment was also able to reduce the IL-1β expression but only down to 0.470 ± 0.233. Similarly for IL-6, the level of expression reduced by 3 times in comparison to foam cells when using MTX-LIP (0.28 ± 0.18) and MTX-SPN (0.2334 ± 0.186) and by 2 times only in the case of free MTX (0.46 ± 0.20). For TNF-α, the effect of MTX-LIP and MTX-SPN, as compared to the free drug, was less significant. Specifically, the TNF-α relative fold expression levels decreased to 0.302 ± 0.080 for the MTX-LIP, 0.138 ± 0.101 for the MTX-SPN, and 0.316 ± 0.186 for the free MTX.

In Figures S9 and S10, data are also provided for the empty LIP and empty SPN. On the genes associated with cholesterol transport, the empty LIP induced only a modest decrease in the level of expression of ABCA1 (0.473 ± 0.162) at 24 h, but in all other conditions the effect of the liposomes was negligible. Very differently, the empty SPNs were observed to downregulate the expression of ABCA1 and upregulate the expression of SRA-1, at both 8 and 24 h. On the pro-inflammatory genes, both nanoparticles increased the expression of IL-1β, IL-6, and TNF-α above the levels measured for BMDM (not exposed to oxLDL). This was indeed expected for the liposomes, but the pro-inflammatory effect was much higher for the empty SPN than for the empty LIP, at all time points and for all genes. This must be related to the low encapsulation efficiency and, consequently, large number of SPN needed to administer the prescribed doses of MTX, which could eventually lead to medium acidification and local inflammation.[40,41]

Before performing animal experiments, the viability of BMDM exposed to different concentrations of MTX and MTX-loaded nanoparticles was assessed via conventional MTT assays. Figure 4C and Figure S11 show the viability of cells treated with free MTX, free DSPE−MTX, MTX-LIP, and MTX-SPN with a drug concentration ranging from 6 nM to 10 μM. Empty LIP and SPN were also tested using a number of particles equivalent to those needed for the delivery of a specific MTX

dose. The IC50 corresponding to the different treatments is provided in the table of Figure 4. DSPE-MTX presented a slightly lower IC50 in comparison to free MTX of 1.04 ± 0.11 μM vs 2.44 ± 0.13 μM. MTX-LIP showed a similar cytotoxicity to the conjugate, with an IC50 = 0.86 ± 0.1, whereas MTX-SPN revealed a slightly higher cytotoxicity with an IC50 of 0.42 ± 0.12 μM. No significant toxicity was observed with empty LIP. Differently from the empty SPN, a toxicity similar to that of MTX-SPN was found. Again, this negative result associated with SPN should be ascribed to the low encapsulation efficiency and large number of particles needed to deliver the required amounts of MTX. Based on these observations, the following preclinical studies were only conducted with MTX-LIP.

Preclinical Characterization of MTX-Liposomes. To directly investigate the effect of MTX-loaded nanoparticles on atherogenesis, apoE$^{-/-}$ mice were subjected to 28 days high fat diet (HFD) to induce lesion development. Mice were concomitantly treated with MTX-LIP or empty LIP for 28 days, with a MTX dose of 2.5 mg administered systemically every 3 days. At the end of the treatment, mice were sacrificed. Major organs were harvested together with the aorta for *ex vivo* analyses. The mice treated with MTX-LIP presented an area of the aortic sinus plaque that was significantly smaller than that detected in control mice, which were treated with empty LIP (Figure 5A). Also, the MTX-LIP treatment had no effect on plaque collagen content (Figure 5B). Analysis on serum samples was also conducted (Figure 5C). No significant differences in total cholesterol were noticed between the two experimental groups. It is therefore unlikely that changes in lipid levels could account for the decreased pathology observed with the MTX-nanoparticle-treated mice. To determine other systemic changes that MTX-LIP may exert on atherosclerosis-driven immune responses, a Luminex analysis was performed to quantify a broad spectrum of cytokines in the serum samples (Figure 5C). A significant ($P < 0.01$) decrease in RANTES (CCL5) was detected. This chemokine is expressed by many hematopoietic and nonhematopoietic cell types and plays an important role in homing and migration of immune cells. A slight increase of IL-1α ($P < 0.05$) was also documented in the MTX-LIP-treated mice (Figure 5C). Concentrations of eotaxin, fibroblast growth factor-basic, granulocyte-macrophage colony-stimulating factor, IFN-γ, IL-1β, IL-2, IL-3, IL-4, IL-5, IL-6, IL-9, IL-10, IL-12 (p40), IL-12 (p70), IL-13, IL-17A, KC, monocyte chemo-attractant protein-1, macrophage inflammatory protein-1α, macrophage inflammatory protein-1β, and tumor necrosis factor-α did not differ significantly between the two experimental groups or were below the level of detection (Table S2). These data may suggest that MTX-LIP mainly exerts a local anti-inflammatory effect with minor systemic implications. This consideration is in accordance with the biodistribution analysis that was performed by immunohistochemistry using Cy5-LIP. These particles maintain the same physiochemical features of the MTX-LIP in terms of size and surface charge. After 24 h of i.v. injection, Cy5-LIP was detected in the spleen and kidneys (Figure 5D), whereas more particles were detected in the liver, as expected, and, more importantly, in the atherosclerotic plaque of the aortic root. A similar distribution was also observed in aged (1 year old) apoE$^{-/-}$ mice with Cy5-LIP clearly detectable in the plaque core and a fibrous cap in the sinus and artic arch, in addition to the kidney and liver (Figure S12). It is here worth noticing that, as previously documented by the authors and other groups,[16,42−44] the percentage of injected nanoparticles accumulating in atherosclerotic plaques upon

systemic administration is minimal as compared to the amounts depositing in organs of the reticuloendothelial system (RES), such as the liver and the spleen. To quantitatively assess particle biodistribution, LIPs were labeled with ^{64}Cu (^{64}Cu-LIP) and injected systemically in healthy mice (C57BL/6). Figure S13A,B documents that the hydrodynamic size of the ^{64}Cu-LIP is comparable to that of MTX-LIP and that the radioisotope ^{64}Cu is firmly conjugated to the LIP surface via the chelating agent DOTA. Figure S13C shows the quantitative biodistribution of the ^{64}Cu-LIP, confirming a significant accumulation in the liver and spleen after 24 h (Figure S13).

■ DISCUSSION

The oxLDL internalization data and the gene expression results presented in Figures 2−4 would suggest that MTX treatments are capable to halt, and possibly reverse, the process of maturation of macrophages into foam cells, which is indeed a pivotal step in the process of atherogenesis and atherosclerosis progression. Overall, MTX treatments have been shown to lower the intracellular deposition of oxLDL in primary rat macrophages mostly by increasing the efflux rates (over-expression of ABCA1) with a modest variation of the influx rates (downregulation of CD36 and SRA-1) (Figures 3 and 4A). In particular, at 8 h, MTX-LIP and MTX-SPN had a different effect on the CD36: MTX-SPN induced a statistically higher reduction in CD36 expression as compared to MTX-LIP. This effect of MTX-LIP on the expression of CD36 should be ascribed to the very nature of the lipid-based particles. Indeed, liposomes do contain cholesterol that could trigger the expression of CD36, as previously reported.[45] MTX treatments appeared to have also a significant effect on modulating inflammation by reducing the production of different cytokines. Especially at 24 h post MTX treatment, the expression of IL-1β, IL-6, and TNF-α went down significantly as compared to the foam cell case (Figure 4B), where inflammation was only induced by direct exposure to oxLDL molecules. Importantly, besides the CD36 expression, the effect of MTX-LIP appeared to be statistically comparable to that of MTX-SPN in most other cases. This demonstrates that the nanoformulations of MTX, even with totally different particles, leads to similar results with a general increase in the expression of genes involved in cholesterol efflux, a decrease in the expression of genes involved in cholesterol influx, and mitigation of the pro-inflammatory cytokine production. Inflammation also represents a pivotal step in atherosclerosis initiation and progression, in that it favors the sustained recruitment of circulating monocytes within vascular lesions and supports their maturation in macrophages and eventually foam cells.[4] The considerable intracellular accumulation of oxLDL in macrophages reduces the ability of the cells to metabolize cholesterol[46] and generate reactive oxygen species triggering and sustaining local inflammation. Thus, controlling both oxLDL transport in and out of cells and the local state of inflammation may have dramatic implications in halting and possibly reversing atherosclerosis.

It is here important to recall that, recently, it was demonstrated that clinical use of low-dose MTX was associated with increased ABCA1 mRNA in peripheral blood mononuclear cells (PBMCs) of rheumatoid arthritis patients.[47] This change in expression in PBMC was closely related to MTX activity.[47] ABCA1 expression is regulated by the adenosine, and MTX promotes adenosine release, thus causing the overexpression of ABCA1.[48] Thus, the efficient delivery of MTX to circulating monocytes and macrophages residing within arterial lesions

could promote the overexpression of ABCA1 and modulate the risks of acute cardiovascular syndromes. However, a low-dose treatment with MTX was not sufficient to mitigate the occurrence of cardiovascular events as demonstrated by the recent failure of CIRT.[10] Indeed, nanoparticles could more efficiently deliver the therapeutic cargo to the biological target, as opposed to the free drug administration, reducing also the risk of adverse effects. Importantly, this work shows that even in vitro the nanoformulated MTX is more effective than free MTX in modulating foam cell formation and alleviating cell inflammation (see Figures 3 and 4).

■ CONCLUSIONS

Two MTX-loaded nanomedicines were designed, realized, and characterized in vitro for their physicochemical and pharmacological properties and in vivo for their ability to modulate atherosclerosis in high-fat-fed apoE$^{-/-}$ mice. The lipid conjugate DSPE-MTX was either dispersed within the hydrophobic PLGA core of spherical polymeric nanoparticles (MTX-SPN) or was integrated in the lipid bilayer of liposomes (MTX-LIP). The encapsulation of the MTX lipid conjugate into MTX-LIP was significantly more efficient than in MTX-SPN.

The ability of MTX to modulate inflammation and regulate the expression of genes involved in the transport of oxLDL was extensively demonstrated using different in vitro assays. In general, possibly because of the higher loading and encapsulation efficiency, MTX-LIP showed a larger impact in reducing the accumulation of oxLDL into macrophages as compared to MTX-SPN and free MTX. This was demonstrated via both confocal fluorescent microscopy and gene expression quantification. Finally, in apoE$^{-/-}$ mice fed a high-fat diet for 28 days, MTX-LIPs were shown to accumulate in atherosclerotic plaques developing within the aortic root. This was accompanied by a significant decrease in circulating levels of RANTES (CCL5), which is an inflammatory chemokine playing a key role in homing and migration of immune cells in the vessel walls, and a significant reduction in atherosclerotic plaque size.

Overall, this work would suggest that MTX-nanoparticles could resuscitate the use of this potent anti-inflammatory drug, or similar therapeutic agents, for the management of atherosclerosis.

■ MATERIALS AND METHODS

Materials. Poly(D,L-lactide-co-glycolide) acid terminated (PLGA, lactide:glycolide 50:50, Mw 38 000−54 000), 1-ethyl-3-(3-(dimethylamino)propyl) carbodiimide (EDC), N-hydroxysuccinimide (NHS), triethylamine (TEA), low-density lipoproteins (LDL), and a cholesterol quantitation kit were purchased from Sigma-Aldrich (St. Louis, MO, USA). Methotrexate (MTX) was bought by AlfaAesar (Haverhill, MA, USA). 1,2-distearoyl-sn-glycero-3-phosphoethanolamine-N-[succinyl(polyethylene glycol)-2000] (DSPE-PEG-COOH), 1,2-distearoyl-sn-glycero-3-phosphoethanolamine (DSPE_NH2), and 1,2-dipalmitoyl-sn-glycero-3-phosphocholine (DPPC) were purchased from Avanti Polar Lipid (Alabaster, AL, USA). All reagents and solvents were used without further purification.

Synthesis of DSPE-MTX. DSPE-MTX was synthesized as reported by Ferreira and co-workers with some modifications.[49] Briefly, MTX was incubated with 1-ethyl-3-(3-(dimethylamino)propyl)carbodiimide (EDC)/N-hydroxysuccinimide (NHS) in dimethyl sulfoxide (DMSO) for 30 min, at room temperature. A solution of DSPE in DMSO was added to the previous solution. A catalytic amount of triethylamine (TEA) was added to the reaction and left to stir for 72 h. The mixture was washed with cold diethyl ether. Finally, the conjugate was lyophilized and stored at −20 °C. Note that free methotrexate (MTX) is soluble solely in a few organic solvents, including DMSO and DMF,

which are toxic and exhibit a very high boiling point (above 150 °C). On the other hand, lipid-MTX can be efficiently separated from an original DMSO solution by using cold diethyl ether and readily used to synthesize particles without employing DMSO or DMF.

Synthesis of SPNs. Spherical polymeric nanoparticles (SPNs) were synthesized by a sonication-emulsion technique method, as described elsewhere.[50] Briefly, carboxyl-terminated poly(lactic-*co*-glycolic acid) (PLGA), DSPE-MTX, and 1,2-dipalmitoyl-*sn*-glycero-3-phosphocholine (DPPC) were dissolved in chloroform in a 5:2:1 ratio to obtain an homogeneous solution (oil phase). The aqueous phase was prepared by dissolving 1,2-distearoyl-*sn*-glycero-3-phosphoethanolamine-*N*-[carboxy(polyethylene glycol)-2000 (DSPE-PEG-COOH) in 4% ethanol. Then, the oil phase was added drop wisely to the aqueous phase under ultrasonication (100% amplitude for 1 min and 30 s). The obtained emulsion was then placed under magnetic stirring to facilitate solvent evaporation. SPNs were centrifuged, first, for 5 min at 1500 rpm to settle down any possible debris, and then the supernatant was centrifuged three more times for 20 min at 12 000 rpm. The pellets were washed in water after every centrifugation step. Different SPN formulations were synthesized (Table S1).

In order to label the SPNs with the near-infrared dye Cy5, a DSPE-Cy5 (0.002 mg) was used instead of DSPE-MTX.

Synthesis of MTX-LIP. Liposomes (LIPs) were prepared by thin-layer evaporation (TLE).[51] Briefly, DPPC, cholesterol, DSPE-PEG, and DSPE-MTX were dissolved in chloroform in a round-bottomed flask (ratio 6:3:1:1). The thin-layer lipid film was obtained with the evaporation of the organic solvent at 60° under reduced pressure. The lipid film was left under the hood overnight to remove any trace of residual solvent. For the production of the multilamellar liposomes, the lipid film was hydrated with 2 mL of HEPES and then subjected to three alternate cycles (3 min each) of warming at 60 °C (thermostated water bath) and vortexing at 700 rpm. The sample was dialysized against HEPES for 1 h. For the preparation of Cy5-LIP, DSPE-Cy5 was used instead of DSPE-MTX. The purification step to remove an excess of Cy-5 was conducted by ultracentrifugation (1 h, 45 000 rpm) instead of dialysis. For the preparation of ^{64}Cu-LIP, 20% w/w of DSPE-PEG was replaced with lipid-DOTA. LIPs were obtained using the previous method. DOTA-LIP was then resuspended in 3 mL of water and 200 μL of acetate buffer (1 mM, pH = 6.0) and conjugated with ^{64}CuCl$_2$ (1 mCi) solution for 2 h at 37 °C. The excess of radioactivity was removed by dialyses against PBS for 1 h.

Characterization of LIPs and SPNs. Liposomes were fixed for 2 h in 2% glutaraldehyde in 0.1 M cacodylate buffer. After fixation, the samples were washed twice with the same buffer and post fixed for 1 h in 1% osmium tetroxide in 0.1 M cacodylate buffer. After several washes with distilled water, samples were subsequently dehydrated in a graded ethanol series, 1:1 ethanol:hexamethyldisilazane (HMDS), and 100% HMDS and dried overnight. Samples were sputtered using gold. SEM images were collected using JEOL JSM-7500FA (Jeol, Tokyo, JAPAN) operating at 5 kV of accelerating voltage. For SPNs, a drop of nanoparticle solution was deposited on a silicon wafer, dried, and mounted on a stab for SEM analysis. The hydrodynamic diameter, polydispersity index, and surface electron ζ-potential of LIP and SPNs were measured using dynamic light scattering (DLS, Malvern Zetasizer Nano S).

Drug Loading and Release. To measure the MTX encapsulation efficiency (EE) and loading efficiency (LE), the samples were lyophilized, dissolved in acetonitrile/H2O (1:1, v/v), and analyzed by high-performance liquid chromatography (HPLC) (Agilent 1260 Infinity, Germany) equipped with a 100 μL sample loop injector. A C18 column (2.1× 250 mm, 5 μm particle size, Agilent, USA) was used for the chromatographic separation. MTX was eluted under isocratic conditions using a binary solvent system [H$_2$O + 0.1% (v/v) TFA, 43:57 v/v] pumped at a flow rate of 1.0 mL/min. The ultraviolet (UV) detection was set at 430 nm.

EE and LE were determined using the following equations:

$$EE\ (\%) = \frac{MTX\ weight\ in\ particles}{MTX\ initial\ feeding\ amount} \times 100$$

$$LE\ (\%) = \frac{MTX\ weight\ in\ particles}{Total\ weight\ of\ the\ particles} \times 100$$

To study MTX and Cy5-release kinetics, 200 μL of MTX-nanoparticle (SPN or LIP) or Cy5-nanoparticles (SPN or LIP) solution was placed into Slide-A-Lyzer MINI dialysis microtubes with a molecular cutoff of 10 kDa (Thermo Scientific) and dialyzed against 4 L of PBS buffer (pH 7.4). For each time point, three samples were collected and dried. For the SPNs, samples were then dissolved in acetonitrile/H$_2$O (1:1, v/v) and analyzed by HPLC. For LIP, samples were destroyed with cold methanol, left to dry, dissolved in acetonitrile/H$_2$O (1:1, v/v), and analyzed by HPLC for the MTX. The experimental data were fitted by using the Ritger−Peppas model for controlled, not swellable drug-delivery systems[52] ($Y = k \times x^n$), where Y represents the drug percentage released; x is the time of observation; and k and n are the fitting parameters.

In the case of Cy-5, after LIP destruction, samples were dissolved in acetonitrile and analyzed by the spectrophotometer at $\lambda = 640$ nm. For ^{64}Cu release, LIPs were analyzed at the γ-counter. The data were normalized taking into account the decay of ^{64}Cu.

LDL Oxidation. LDLs (2 mg/mL) were incubated with 5 mM CuSO$_4$ at 37 °C for 4 h without EDTA. The reaction was interrupted with the addition of EDTA (5 mM). The formed oxidized LDL molecules (oxLDL) were dialyzed against PBS containing 0.01% EDTA at 4 °C for 24 h and stored at 4 °C.[53] The fluorophore 1,1′-dioctadecyl-3,3,3′,3′-tetramethylindocarbocyanine perchlorate (Dil) was used for fluorescently tagging the lipoprotein following a previously published protocol.[54] Briefly, Dil was preincubated with LDL overnight at 37 °C under agitation. Dil-LDL was then oxidized and ultracentrifuged for 5 h at 45 000 rpm and 4° in order to remove unbound fluorophore. The obtained Dil-oxLDL were dialyzed against PBS containing 0.01% EDTA at 4 °C for 24 h and stored at 4 °C.

Bone Marrow Derived Macrophages. For bone marrow derived macrophages (BMDMs), rat femurs were explanted, and the extremities were cut off. Then, the bone marrow canal was flushed four times with 500 μL of medium. The resulting cell suspension was filtered using 70 μm cell strainers. Cells were seeded in a Petri dish, and medium was changed after 3 days to remove unattached cells. BMDMs were used on the following day. BMDMs were cultured in DMEM supplemented with 15% FBS, 1% penicillin/streptomycin, and rat M-CSF (according to vendor indications). Cells were cultured under controlled environmental conditions (37 °C in 5% CO$_2$).

Foam Cell Formation and Cholesterol Quantification. BMDM/Raw 264.7 cells were cultured in DMEM containing, respectively, 15% and 10% fetal bovine serum (FBS), 1% antibiotic (penicillin/streptomycin), and 1% glutamine. Cells were seeded at a density of 1×10^5 cells/mL. For foam cells, the formation of different amounts of oxLDL was tested (0, 20, 50, and 80 μg/mL of oxLDL). Macrophages were incubated with oxLDL overnight; the medium was removed; and cells were washed twice with PBS and fixed with a solution of paraformaldehyde of 3.7% (PFA). Macrophages were incubated with isopropanol and Oil Red O (ORO) working solution for 10−20 min. Cells were observed with a microscope (Leica 5500), and images were acquired with a 20× magnification.[55]

Confocal Fluorescent Microscopy Imaging. Confocal images of RAW 267.4 were obtained using a Nikon-A1 confocal microscope (Nikon Corporation, Japan). Free Dil or Dil-oxLDL (0.15 mg of Dil: 6.5 mg of LDL) were incubated with macrophages overnight. A number of 50 000 cells (either Raw267.4 or BMDM) were seeded into each well of a Nunc Lab-Tek II Chamber Slide System (Thermo Fisher Scientific, USA), maintaining culturing conditions, as described for foam cell formation and cholesterol quantification protocols. After 14 h, the culturing media was removed, and cells were washed in PBS (Thermo Fisher Scientific, USA). Fixation was performed using a 3.7% solution of PFA (Sigma-Aldrich, USA) for 5 min. Lysosomes were stained with LysoTracker Green (Thermo Fisher Scientific, USA) and nuclei with DAPI (Thermo Fisher Scientific, USA) following the vendor indications. A z-stack section was acquired using a 60× objective (≥12 steps of 1000 nm each were acquired per image).

Time Lapse Microscopy Analysis. For time lapse microscopy experiments, 20 000 BMDMs were seeded into a Nunc Lab-Tek II Chamber Slide System (Thermo Fisher Scientific, USA). The same experimental conditions were used: BMDMs were incubated overnight with 50 μg/mL of Dil-oxLDL and an equal amount of Dil. The experiment was performed using a Nikon Eclipse-Ti-E microscope (Nikon Corporation, Japan). During the image acquisition, cells were kept in controlled environmental conditions: 37 °C in a humidified 5% CO_2 atmosphere. Movies were acquired at a frame rate of 80 fps using a 60× objective.

Analysis of Dil-oxLDL Uptake and Expulsion. After inducing the transformation of BMDM in foam cells with Dil-oxLDL, cells were treated for 24 h with 0.16 μM of free MTX, empty nanoparticles, and MTX nanoparticles. At the end of the treatment, the medium was removed, and cells were washed twice with PBS. Cell fixation was performed using a 3.7% solution of PFA (Sigma-Aldrich, USA) for 15 min. Actin was stained with Alexa Fluor 488 Phalloidin (Thermo Fisher Scientific, USA) and nuclei with DAPI (Thermo Fisher Scientific, USA), following the vendor's indications. Data were analyzed with ImageJ.

Cholesterol Quantification. BMDM total cholesterol (free cholesterol and cholesteryl ester) was quantified using a Cholesterol Quantitation Kit (Sigma-Aldrich, Italy), following the manufacturer's instruction. First, cells were treated with oxLDL and then with free MTX and MTX-loaded nanoparticles as described previously. Cholesterol quantification was normalized on the total amount of protein calculated using a Pierce Brentford Protein Assay Kit (Thermos Scientific).

TEM Characterization. Transmission electron microscopy (TEM) micrographs were acquired using a JEOL JEM 1011 (Jeol, Japan) electron microscope operating with an acceleration voltage of 100 kV and recorded with an 11 MegaPixel fiber optical charge-coupled device (CCD) camera (Gatan Orius SC-1000). LDL was diluted 1:100, dropped on 150-mesh glow discharged "Ultrathin" carbon-coated copper TEM grids, and dried. Dried TEM samples were negatively stained using 2% uranyl acetate aqueous solution. In order to observe LDL uptake in foam cells, RAW 264.7 cells were cultured and treated on glass coverslips. Samples were fixed for 2 h in 1.5% glutaraldehyde in 0.1 M sodium cacodylate buffer (pH 7.4), post fixed in 1% osmium tetroxide in the same buffer, and stained overnight with 1% uranyl acetate aqueous solution. Samples were then dehydrated in a graded ethanol series, infiltrated with series of ethanol/resin solution, and finally embedded in epoxy resin (Epon 812, TAAB). Thin sections were cut with the Leica UC6 ultramicrotome (Leica Microsystems, Germany), equipped with a diamond knife (Diatome). In order to better localize the fluorescent LDL molecules inside cells, LDL uptake in foam cells was investigated by means of correlative light and electron microscopy. Foam cells were cultured and treated on grid-etched glass coverslips. After fluorescence microscopy observation, samples were fixed for 1.5 h in 4% paraformaldehyde (PFA) and 0.2% glutaraldehyde solution prepared in 0.1 M phosphate buffer. Fluorescence images were acquired using a Nikon-A1 confocal microscope (Nikon Corporation, Japan). Dil-oxLDL was used for the treatment. The nuclei were stained with DAPI and the lysosomes with the LysoTracker Green (Thermo Fisher Scientific, USA). After fluorescence observation, foam cells were processed for TEM analysis as described above, using reference marks. Image analysis and merging were performed using the PhotoShop image processing software.

Gene Expression and Toxicity. BMDMs were cultured at 37 °C in 5% CO_2, in high-glucose DMEM, and supplemented with 15% FBS and 1% L-glutamine, according to ATCC instructions. Cells were seeded into 96-well plates at a density of 20×10^3 cells per well and incubated for 24, 48, and 72 h. Cells were treated with different concentrations of free MTX, DSPE-MTX, MTX-SPNs, MTX-LIP (namely, 0.0064, 0.032, 0.16, 0.8, 4, 10, and 0 μM of MTX) or empty SPNs/LIP. The MTT solution was added for 4 h, and the formed formazan crystals were dissolved in ethanol. Absorbance was measured at 570 nm, using 650 nm as the reference wavelength (Tecan, Männedorf, Swiss). The percentage of cell viability was assessed according to the following equation:

$$\text{Cell viability}(\%) = \frac{\text{Abs}_T}{\text{Abs}_C} \times 100$$

where Abs_T is the absorbance of treated cells and Abs_C is the absorbance of untreated cells (control).

The anti-inflammatory effects of MTX, MTX-SPNs, and MTX-LIP were tested on foam cells at 8 and 24 h by measuring gene expression of three pro-inflammatory cytokines, namely, tumor necrosis factor-α (TNF-α), interleukin-1β (IL-1β), and interleukin-6 (IL-6) in rat BMDMs.

The gene expression of foam cells markers (CD36 and SRA-1) and cholesterol expulsion ATP-binding cassette transporter 1 (ABCA1) was also assessed. Cells were cultured under controlled environmental conditions (37 °C in 5% CO_2) and seeded into 6-well plates at a density of 4×10^5 cells per well. After 10 h, BMDMs were incubated with oxLDL overnight. Cells were treated with MTX nanoparticles at 0.16 μM of MTX and incubated for 8 and 24 h. RNA was extracted using a RNAeasy Plus Mini Kit (Qiagen) and quantified by NanoDrop2000 (Thermo Scientific, Waltham, Massachusetts, USA). Three independent biological replicates were run using a Power SYBR Green RNA-to-CT 1-Step Kit (Applied Biosystems) and using GAPDH gene expression as a housekeeping gene. Reactions were performed in a final volume of 10 μL. Primer pair sequences are listed below: GAPDH: 5'-CATCACTGCCACCCAGAAGACTG-3' and 5'-ATGCCAGT-GAGCTTCCCGTTCAG-3'; TNF-α: 5'-GGTGCCTATGTCT-CAGCCTCTT-3' and 5'-GCCATAGAACTGATGAGAGGGAG-3'; IL-1β: 5'-AACCTGCTGGTGTGTGACGTTC-3' and 5'-CAGCAC-GAGGCTTTTTTGTTGT-3'; IL-6:5'-TACCACTTCACAAGTCG-GAGGC-3' and 5'-CTGCAAGTGCATCATCGTTGTTC-3'; CD36:5'-ATGGGCTGTGATCGGAACTG-3' and 5'-GTCTTCCCAATAAGCATGTCTCC-3'; SRA-1:5'-CTGA-GACCTCTGGAACAGGCAT-3' and 5'-TGCACTAGCAGTGC-CATCCTCT-3'; and ABCA1:5'-GGAGCCTTTGTG-GAACTCTTCC-3' and 5'-CGCTCTCTTCAGCCACTTTGAG-3'.

Internalization Study. Flow cytometry was performed using a FACS ARIA (Becton Dickinson, USA). A number of 200 000 macrophages/foam cells were seeded into each well of a 12-well plate maintaining culturing conditions indicated in foam cell formation and cholesterol quantification protocol. Cells were treated for 2, 8, and 24 h with Cy5-LIP and Cy5-SPNs. After treatment, cells were washed using cold PBS in order to facilitate the scraping procedures. After washing, a volume of 200 μL of PBS was used to detach the cells by gentle scraping the plastic bottom. Samples were immediately stored in ice and vortexed right before the analysis. A cell population was selected setting a scatter gate that would exclude the negligible amounts of debris and aggregates while taking into account the side scatter (SSC) shift due to internal complexity changes caused by the internalized particles. The cell population positive for internalization was selected considering the basal level of fluorescence in untreated cells.

Animals. B6.129P2-Apoe(tm1Unc)/J (apoE$^{-/-}$) mice were bred in-house (Central Research Facility, University of Glasgow). Animals were maintained on a 12/12 h light/dark cycle with free access to food and water. All the procedures were performed in accordance with local ethical and UK Home Office regulations. Twelve-week-old male apoE$^{-/-}$ mice were fed with high-fat diet (HFD) (Western RD diet, 21% fat, 0.2% cholesterol, supplemented with 150 ppm fenbendazole, Diet code: 823963 - Special Diet Services, Essex, UK) for 28 days. Empty or MTX-LIP (2.5 mg/kg) was injected intravenously (i.v.), administered starting from day 0 every third day. Mice were culled at 28 days, and samples were processed as described below. At the end of the experimental protocol mice were perfused with ice cold PBS; the heart was embedded in Tissue-Tec OCT (Tissue Tek, Sakura Finetek Europe, Zoeterwoude, The Netherlands), frozen at −80 °C, and sectioned (10 μm). Aortic sinus sections were stained with oil red O counterstained with hematoxylin. Picrosirius red viewed with polarized light was used to detect collagen. For each animal, 10 sections were analyzed to determine atherosclerotic lesion size, and four sections were analyzed to determine the collagen content, as previously described.[56] The analyses were carried out using ImageJ software (National Institutes of Health Imaging; http://rsbweb.nih.gov/ij), and the results

are expressed as the mean lesion area and mean percentage collagen area.

Cytokine Detection Assays. Concentrations of eotaxin, fibroblast growth factor-basic, granulocyte-macrophage colony-stimulating factor, IFN-γ, interleukin (IL)-1α, IL-1β, IL-2, IL-3, IL-4, IL-5, IL-6, IL-9, IL-10, IL-12 (p40), IL-12 (p70) IL-13, IL-17A, KC, monocyte chemoattractant protein-1, macrophage inflammatory protein-1α, macrophage inflammatory protein-1β, RANTES (Regulated on Activation, Normal T Cell Expressed and Secreted), and tumor necrosis factor-α were assessed in serum using a Bio-Plex Pro Mouse Cytokine 23-plex Assay, according to the manufacturer's instructions (Bio-Rad), and analyzed using a Bio-Rad Luminex 200 Plate Reader (Hemel Hempstead, United Kingdom). Data were analyzed using Bio-Plex 6.1 software with 5PL curve fitting.

Immunohistochemical Analysis. To determine nanoparticle distribution, apoE$^{-/-}$ mice were culled 24 h after the final injection of fluorescent Cy-5-LIP (the amount of particle used was equivalent to the one used for one injection of MTX-LIP). The aortic sinus, spleen, kidney, and liver were dissected, embedded in OCT (Tissue Tek, Sakura Finetek Europe, Zoeterwoude, The Netherlands), and snap frozen for immunohistochemical analysis. Sections of 10 μm were cut. For staining, sections were fixed in acetone for 10 min, air-dried, and rehydrated with PBS before incubation in serum-free Protein Block (DakoCytomation, Glostrup, Denmark) for 30 min. Aortic sinus sections were incubated with FITC-conjugated anti-α-SMA antibodies. Hoechst was used to identify nuclei as previously described.[57] Images were acquired using a Zeiss Cell Observer SD confocal microscope (Zeiss, Oberkochen, Germany).

Serum Lipid Analysis. Measurements of mouse blood total cholesterol levels were performed with the cholesterol/cholesteryl ester quantitation kit (ab65359, Abcam, Toronto, ON) according to the manufacturer's instructions.

Biodistribution of LIP in Naïve Mice. LIPs labeled with Cu^{64} were injected in 5 naïve mice (C57BL/6). At 24 h post injection, the mice were sacrificed, and the major organs (liver, spleen, kidneys, intestine, brain, lungs, and heart) were explanted and analyzed for their radioactive activity at the γ-counter. The data were then normalized for the weight of the organs.

Statistical Analysis. All the *in vitro* data were represented as the average $\pm$ standard deviation (SD) of three different measurements, unless differently specified. The statistical significant difference was assessed using an ANOVA test, with Bonferroni's Multiples Comparison Test as a posthoc test. All statistical *in vitro* analyses were performed using GraphPad Prism v.5 (GraphPad Software, USA). *In vivo* results are expressed as mean $\pm$ SEM of the number of animals. Normality distribution was tested, and a Student *t* test was used to compare two groups. All statistical *in vivo* analyses were performed using GraphPad Prism v.7 (GraphPad Software, USA). A *p* value ≤ 0.05 was considered statistically significant.

■ ASSOCIATED CONTENT

ⓢ Supporting Information

The Supporting Information is available free of charge at https://pubs.acs.org/doi/10.1021/acsami.0c12202.

DSPE-MTX prodrug synthesis; MTX-loaded nanoparticle stability under slightly acidic conditions; MTX-SPN optimization; oxidized low-density lipoproteins (oxLDL) characterization; intracellular localization of oxLDL; stable association of Dil and oxLDL molecules; DLS analysis and release study of Cy5-LIP and Cy5-SPN; expression levels for the genes regulating the cholesterol transport; expression levels for the genes associated with the anti-inflammatory cytokines; viability of BMDM incubated with MTX, DSPE-MTX, empty SPN, MTX-SPN, and empty LIP at 3 different time points; luminex results; representative biodistribution confocal imaging after injection of Cy5-liposomes in an one-year-old female apoE$^{-/-}$ mouse. Biodistribution study with ^{64}Cu-LIP on C57BL/6J mice (PDF)

Trafficking of Dil-oxLDL (AVI)

Cellular membrane staining (AVI)

■ AUTHOR INFORMATION

Corresponding Author

Paolo Decuzzi — *Laboratory of Nanotechnology for Precision Medicine, Fondazione Istituto Italiano di Tecnologia, 16163 Genoa, Italy;* ⓞ orcid.org/0000-0001-6050-4188; Email: paolo.decuzzi@iit.it

Authors

Valentina Di Francesco — *Laboratory of Nanotechnology for Precision Medicine, Fondazione Istituto Italiano di Tecnologia, 16163 Genoa, Italy; Department of Informatics, Bioengineering, Robotics and System Engineering, University of Genoa, 16145 Genoa, Italy;* ⓞ orcid.org/0000-0003-4216-724X

Danila Gurgone — *Centre for Immunobiology, Institute of Infection, Immunity and Inflammation, College of Medical, Veterinary and Life Sciences, University of Glasgow, Glasgow G12 8TA, United Kingdom; Department of Pharmacy, University of Naples Federico II, Naples 80131, Italy;* ⓞ orcid.org/0000-0001-7736-1187

Roberto Palomba — *Laboratory of Nanotechnology for Precision Medicine, Fondazione Istituto Italiano di Tecnologia, 16163 Genoa, Italy;* ⓞ orcid.org/0000-0002-9715-3876

Miguel Filipe Moreira Marques Ferreira — *Laboratory of Nanotechnology for Precision Medicine, Fondazione Istituto Italiano di Tecnologia, 16163 Genoa, Italy;* ⓞ orcid.org/0000-0002-1560-3571

Tiziano Catelani — *Electron Microscopy Facility, Istituto Italiano di Tecnologia, Genova 16163, Italy;* ⓞ orcid.org/0000-0002-3790-5749

Antonio Cervadoro — *Laboratory of Nanotechnology for Precision Medicine, Fondazione Istituto Italiano di Tecnologia, 16163 Genoa, Italy;* ⓞ orcid.org/0000-0003-3087-2363

Pasquale Maffia — *Centre for Immunobiology, Institute of Infection, Immunity and Inflammation, College of Medical, Veterinary and Life Sciences and Institute of Cardiovascular and Medical Sciences, College of Medical, Veterinary and Life Sciences, University of Glasgow, Glasgow G12 8TA, United Kingdom; Department of Pharmacy, University of Naples Federico II, Naples 80131, Italy;* ⓞ orcid.org/0000-0003-3926-4225

Complete contact information is available at:
https://pubs.acs.org/10.1021/acsami.0c12202

Author Contributions

¶P.M. and P.D. have a shared senior authorship.

Notes

The authors declare no competing financial interest.

■ REFERENCES

(1) Libby, P.; Hansson, G. K. Taming Immune and Inflammatory Responses to Treat Atherosclerosis. *Journal of the American College of Cardiology* **2018**.

(2) Kim, Y.; Lobatto, M. E.; Kawahara, T.; Lee Chung, B.; Mieszawska, A. J.; Sanchez-Gaytan, B. L.; Fay, F.; Senders, M. L.; Calcagno, C.; Becraft, J.; Tun Saung, M.; Gordon, R. E.; Stroes, E. S. G.; Ma, M.; Farokhzad, O. C.; Fayad, Z. A.; Mulder, W. J. M.; Langer, R. Probing Nanoparticle Translocation across the Permeable Endothelium in Experimental Atherosclerosis. *Proc. Natl. Acad. Sci. U. S. A.* **2014**, *111*, 1078−1083.

(3) Moore, K. J.; Tabas, I. Macrophages in the Pathogenesis of Atherosclerosis. *Cell* **2011**, *145*, 341−355.

(4) Welsh, P.; Grassia, G.; Botha, S.; Sattar, N.; Maffia, P. Targeting Inflammation to Reduce Cardiovascular Disease Risk: A Realistic Clinical Prospect? *British journal of pharmacology* **2017**, *174*, 3898−3913.

(5) Ridker, P. M.; Everett, B. M.; Thuren, T.; MacFadyen, J. G.; Chang, W. H.; Ballantyne, C.; Fonseca, F.; Nicolau, J.; Koenig, W.; Anker, S. D.; et al. Antiinflammatory Therapy with Canakinumab for Atherosclerotic Disease. *N. Engl. J. Med.* **2017**, *377*, 1119−1131.

(6) Weber, C.; Noels, H. Atherosclerosis: Current Pathogenesis and Therapeutic Options. *Nat. Med.* **2011**, *17*, 1410.

(7) Cronstein, B. N.; Naime, D.; Ostad, E. The Antiinflammatory Mechanism of Methotrexate. Increased Adenosine Release at Inflamed Sites Diminishes Leukocyte Accumulation in an in Vivo Model of Inflammation. *J. Clin. Invest.* **1993**, *92*, 2675−2682.

(8) Hasko, G.; Cronstein, B. Regulation of Inflammation by Adenosine. *Front. Immunol.* **2013**, *4*, 85.

(9) Balanescu, A. R.; Bojinca, V. C.; Bojinca, M.; Donisan, T.; Balanescu, S. M. Cardiovascular Effects of Methotrexate in Immune-Mediated Inflammatory Diseases. *Exp. Ther. Med.* **2018**, *17*, 1024−1029.

(10) Ridker, P. M.; Everett, B. M.; Pradhan, A.; MacFadyen, J. G.; Solomon, D. H.; Zaharris, E.; Mam, V.; Hasan, A.; Rosenberg, Y.; Iturriaga, E.; et al. Low-Dose Methotrexate for the Prevention of Atherosclerotic Events. *N. Engl. J. Med.* **2019**, *380*, 752−762.

(11) Kivity, S.; Zafrir, Y.; Loebstein, R.; Pauzner, R.; Mouallem, M.; Mayan, H. Clinical Characteristics and Risk Factors for Low Dose Methotrexate Toxicity: A Cohort of 28 Patients. *Autoimmun. Rev.* **2014**, *13*, 1109−1113.

(12) Chen, M.; Daddy, J.; Amerigos, K.; Su, Z.; Guissi, N. E. I.; Xiao, Y.; Zong, L.; Ping, Q. Folate Receptor-Targeting and Reactive Oxygen Species-Responsive Liposomal Formulation of Methotrexate for Treatment of Rheumatoid Arthritis. *Pharmaceutics* **2019**, *11*, 582.

(13) Alekseeva, A. A.; Moiseeva, E. V.; Onishchenko, N. R.; Boldyrev, I. A.; Singin, A. S.; Budko, A. P.; Shprakh, Z. S.; Molotkovsky, J. G.; Vodovozova, E. L. Liposomal Formulation of a Methotrexate Lipophilic Prodrug: Assessment in Tumor Cells and Mouse T-Cell Leukemic Lymphoma. *Int. J. Nanomed.* **2017**, *12*, 3735.

(14) Maranhao, R.; Guido, M. C.; Derisio de Lima, A.; Rufo Tavares, E.; Franca Marques, A.; Dantas Tavares de Melo, M.; Nicolau, J. C.; Salemi, V.; Kalil-Filho, R. Methotrexate Carried in Lipid Core Nanoparticles Reduces Myocardial Infarction Size and Improves Cardiac Function in Rats. *Int. J. Nanomed.* **2017**, *12*, 3767.

(15) Bulgarelli, A.; Leite, A. C.; Dias, A. A.; Maranhão, R. C. Anti-Atherogenic Effects of Methotrexate Carried by a Lipid Nanoemulsion That Binds to Ldl Receptors in Cholesterol-Fed Rabbits. *Cardiovasc. Drugs Ther.* **2013**, *27*, 531−539.

(16) Stigliano, C.; Ramirez, M. R.; Singh, J. V.; Aryal, S.; Key, J.; Blanco, E.; Decuzzi, P. Methotraxate-Loaded Hybrid Nanoconstructs Target Vascular Lesions and Inhibit Atherosclerosis Progression in Apoe−/− Mice. *Adv. Healthcare Mater.* **2017**, *6*, 1601286.

(17) Robbins, C. S.; Hilgendorf, I.; Weber, G. F.; Theurl, I.; Iwamoto, Y.; Figueiredo, J.-L.; Gorbatov, R.; Sukhova, G. K.; Gerhardt, L. M.; Smyth, D.; et al. Local Proliferation Dominates Lesional Macrophage Accumulation in Atherosclerosis. *Nat. Med.* **2013**, *19*, 1166.

(18) Beldman, T. J.; Senders, M. L.; Alaarg, A.; Pérez-Medina, C.; Tang, J.; Zhao, Y.; Fay, F.; Deichmöller, J.; Born, B.; Desclos, E.; et al. Hyaluronan Nanoparticles Selectively Target Plaque-Associated Macrophages and Improve Plaque Stability in Atherosclerosis. *ACS Nano* **2017**, *11*, 5785−5799.

(19) Zhang, L.; Tian, X. Y.; Chan, C. K.; Bai, Q.; Cheng, C. K.; Chen, F. M.; Cheung, M. S.; Yin, B.; Yang, H.; Yung, W.-Y.; et al. Promoting the Delivery of Nanoparticles to Atherosclerotic Plaques by DNA Coating. *ACS Appl. Mater. Interfaces* **2019**, *11*, 13888−13904.

(20) Davies, P. F. Hemodynamic Shear Stress and the Endothelium in Cardiovascular Pathophysiology. *Nat. Clin. Pract. Cardiovasc. Med.* **2009**, *6*, 16.

(21) Taylor, C. A.; Hughes, T. J.; Zarins, C. K. Finite Element Modeling of Three-Dimensional Pulsatile Flow in the Abdominal Aorta: Relevance to Atherosclerosis. *Ann. Biomed. Eng.* **1998**, *26*, 975−987.

(22) Hossain, S. S.; Hughes, T. J.; Decuzzi, P. Vascular Deposition Patterns for Nanoparticles in an Inflamed Patient-Specific Arterial Tree. *Biomech. Model. Mechanobiol.* **2014**, *13*, 585−597.

(23) Charoenphol, P.; Mocherla, S.; Bouis, D.; Namdee, K.; Pinsky, D. J.; Eniola-Adefeso, O. Targeting Therapeutics to the Vascular Wall in Atherosclerosis−Carrier Size Matters. *Atherosclerosis* **2011**, *217*, 364−370.

(24) Beldman, T. J.; Malinova, T. S.; Desclos, E.; Grootemaat, A. E.; Misiak, A. L.; van der Velden, S.; van Roomen, C. P.; Beckers, L.; van Veen, H. A.; Krawczyk, P. M.; et al. Nanoparticle-Aided Characterization of Arterial Endothelial Architecture During Atherosclerosis Progression and Metabolic Therapy. *ACS Nano* **2019**, *13*, 13759−13774.

(25) Wei, X.; Ying, M.; Dehaini, D.; Su, Y.; Kroll, A. V.; Zhou, J.; Gao, W.; Fang, R. H.; Chien, S.; Zhang, L. Nanoparticle Functionalization with Platelet Membrane Enables Multifactored Biological Targeting and Detection of Atherosclerosis. *ACS Nano* **2018**, *12*, 109−116.

(26) Kheirolomoom, A.; Kim, C. W.; Seo, J. W.; Kumar, S.; Son, D. J.; Gagnon, M. K. J.; Ingham, E. S.; Ferrara, K. W.; Jo, H. Multifunctional Nanoparticles Facilitate Molecular Targeting and Mirna Delivery to Inhibit Atherosclerosis in Apoe−/−Mice. *ACS Nano* **2015**, *9*, 8885−8897.

(27) Ye, M.; Zhou, J.; Zhong, Y.; Xu, J.; Hou, J.; Wang, X.; Wang, Z.; Guo, D. Sr-a-Targeted Phase-Transition Nanoparticles for the Detection and Treatment of Atherosclerotic Vulnerable Plaques. *ACS Appl. Mater. Interfaces* **2019**, *11*, 9702−9715.

(28) Liu, Y.; Luehmann, H. P.; Detering, L.; Pressly, E. D.; McGrath, A. J.; Sultan, D.; Nguyen, A.; Grathwohl, S.; Shokeen, M.; Zayed, M.; et al. Assessment of Targeted Nanoparticle Assemblies for Atherosclerosis Imaging with Positron Emission Tomography and Potential for Clinical Translation. *ACS Appl. Mater. Interfaces* **2019**, *11*, 15316−15321.

(29) Nahrendorf, M.; Zhang, H.; Hembrador, S.; Panizzi, P.; Sosnovik, D. E.; Aikawa, E.; Libby, P.; Swirski, F. K.; Weissleder, R. Nanoparticle Pet-Ct Imaging of Macrophages in Inflammatory Atherosclerosis. *Circulation* **2008**, *117*, 379.

(30) Flores, A. M.; Hosseini-Nassab, N.; Jarr, K.-U.; Ye, J.; Zhu, X.; Wirka, R.; Koh, A. L.; Tsantilas, P.; Wang, Y.; Nanda, V.; et al. Pro-Efferocytic Nanoparticles Are Specifically Taken up by Lesional Macrophages and Prevent Atherosclerosis. *Nat. Nanotechnol.* **2020**, *15*, 154−161.

(31) Moshikur, R. M.; Chowdhury, M. R.; Wakabayashi, R.; Tahara, Y.; Moniruzzaman, M.; Goto, M. Ionic Liquids with Methotrexate Moieties as a Potential Anticancer Prodrug: Synthesis, Characterization and Solubility Evaluation. *J. Mol. Liq.* **2019**, *278*, 226−233.

(32) Tishler, M.; Caspi, D.; Graff, E.; Segal, R.; Peretz, H.; Yaron, M. Synovial and Serum Levels of Methotrexate During Methotrexate Therapy of Rheumatoid Arthritis. *Rheumatology* **1989**, *28*, 422−423.

(33) Lee, A.; Di Mascolo, D.; Francardi, M.; Piccardi, F.; Bandiera, T.; Decuzzi, P. Spherical Polymeric Nanoconstructs for Combined Chemotherapeutic and Anti-Inflammatory Therapies. *Nanomedicine* **2016**, *12*, 2139−2147.

(34) Santarella-Mellwig, R.; Haselmann, U.; Schieber, N. L.; Walther, P.; Schwab, Y.; Antony, C.; Bartenschlager, R.; Romero-Brey, I. Correlative Light Electron Microscopy (Clem) for Tracking and Imaging Viral Protein Associated Structures in Cryo-Immobilized Cells. *J. Visualized Exp.* **2018**, No. e58154.

(35) Pulanco, M. C.; Cosman, J.; Ho, M.-M.; Huynh, J.; Fing, K.; Turcu, J.; Fraser, D. A. Complement Protein C1q Enhances Macrophage Foam Cell Survival and Efferocytosis. *J. Immunol.* **2017**, *198*, 472−480.

(36) Yokode, M.; Kita, T.; Kikawa, Y.; Ogorochi, T.; Narumiya, S.; Kawai, C. Stimulated Arachidonate Metabolism During Foam Cell Transformation of Mouse Peritoneal Macrophages with Oxidized Low Density Lipoprotein. *J. Clin. Invest.* **1988**, *81*, 720−729.

(37) Lu, S. M.; Fairn, G. D. 7-Ketocholesterol Impairs Phagocytosis and Efferocytosis Via Dysregulation of Phosphatidylinositol 4, 5-Bisphosphate. *Traffic* **2018**, *19*, 591−604.

(38) Reiss, A. B.; Carsons, S. E.; Anwar, K.; Rao, S.; Edelman, S. D.; Zhang, H.; Fernandez, P.; Cronstein, B. N.; Chan, E. S. Atheroprotective Effects of Methotrexate on Reverse Cholesterol Transport Proteins and Foam Cell Transformation in Human Thp-1 Monocyte/Macrophages. *Arthritis Rheum.* **2008**, *58*, 3675−3683.

(39) Nicholson, A. C.; Hajjar, D. P. Cd36, Oxidized Ldl and Ppar Gamma: Pathological Interactions in Macrophages and Atherosclerosis. *Vasc. Pharmacol.* **2004**, *41*, 139.

(40) Di Mascolo, D.; Lyon, C. J.; Aryal, S.; Ramirez, M. R.; Wang, J.; Candeloro, P.; Guindani, M.; Hsueh, W. A.; Decuzzi, P. Rosiglitazone-Loaded Nanospheres for Modulating Macrophage-Specific Inflammation in Obesity. *J. Controlled Release* **2013**, *170*, 460−468.

(41) Conniot, J.; Scomparin, A.; Peres, C.; Yeini, E.; Pozzi, S.; Matos, A. I.; Kleiner, R.; Moura, L. I.; Zupančič, E.; Viana, A. S.; et al. Immunization with Mannosylated Nanovaccines and Inhibition of the Immune-Suppressing Microenvironment Sensitizes Melanoma to Immune Checkpoint Modulators. *Nat. Nanotechnol.* **2019**, *14*, 891−901.

(42) Alaarg, A.; Senders, M. L.; Varela-Moreira, A.; Perez-Medina, C.; Zhao, Y.; Tang, J.; Fay, F.; Reiner, T.; Fayad, Z. A.; Hennink, W. E.; Metselaar, J. M.; Mulder, W. J. M.; Storm, G. A Systematic Comparison of Clinically Viable Nanomedicines Targeting Hmg-Coa Reductase in Inflammatory Atherosclerosis. *J. Controlled Release* **2017**, *262*, 47−57.

(43) Beldman, T. J.; Senders, M. L.; Alaarg, A.; Perez-Medina, C.; Tang, J.; Zhao, Y.; Fay, F.; Deichmoller, J.; Born, B.; Desclos, E.; van der Wel, N. N.; Hoebe, R. A.; Kohen, F.; Kartvelishvily, E.; Neeman, M.; Reiner, T.; Calcagno, C.; Fayad, Z. A.; de Winther, M. P. J.; Lutgens, E.; Mulder, W. J. M.; Kluza, E. Hyaluronan Nanoparticles Selectively Target Plaque-Associated Macrophages and Improve Plaque Stability in Atherosclerosis. *ACS Nano* **2017**, *11*, 5785−5799.

(44) Tang, J.; Baxter, S.; Menon, A.; Alaarg, A.; Sanchez-Gaytan, B. L.; Fay, F.; Zhao, Y.; Ouimet, M.; Braza, M. S.; Longo, V. A.; Abdel-Atti, D.; Duivenvoorden, R.; Calcagno, C.; Storm, G.; Tsimikas, S.; Moore, K. J.; Swirski, F. K.; Nahrendorf, M.; Fisher, E. A.; Perez-Medina, C.; Fayad, Z. A.; Reiner, T.; Mulder, W. J. Immune Cell Screening of a Nanoparticle Library Improves Atherosclerosis Therapy. *Proc. Natl. Acad. Sci. U. S. A.* **2016**, *113*, E6731−E6740.

(45) Han, J.; Hajjar, D. P.; Febbraio, M.; Nicholson, A. C. Native and Modified Low Density Lipoproteins Increase the Functional Expression of the Macrophage Class B Scavenger Receptor, Cd36. *J. Biol. Chem.* **1997**, *272*, 21654−21659.

(46) Volobueva, A.; Zhang, D.; Grechko, A. V.; Orekhov, A. N. Foam Cell Formation and Cholesterol Trafficking and Metabolism Disturbances in Atherosclerosis. *Cor Vasa* **2019**, *61*, 48.

(47) Chen, D.-Y.; Chih, H.-M.; Lan, J.-L.; Chang, H.-Y.; Chen, W.-W.; Chiang, E.-P. I. Blood Lipid Profiles and Peripheral Blood Mononuclear Cell Cholesterol Metabolism Gene Expression in Patients with and without Methotrexate Treatment. *BMC Med.* **2011**, *9*, 4.

(48) Coomes, E.; Chan, E. S.; Reiss, A. B. Methotrexate in Atherogenesis and Cholesterol Metabolism. *Cholesterol* **2011**, *2011*, 1.

(49) Ferreira, M.; Rizzuti, I. F.; Palange, A. L.; Barbato, M. G.; Di Francesco, V.; Di Francesco, M.; Decuzzi, P. Optimizing the Pharmacological Properties of Discoidal Polymeric Nanoconstructs against Triple Negative Breast Cancer Cells. *Front. Bioeng. Biotechnol.* **2020**, *8*, 5.

(50) Lee, A.; De Mei, C.; Fereira, M.; Marotta, R.; Yoon, H. Y.; Kim, K.; Kwon, I. C.; Decuzzi, P. Dexamethasone-Loaded Polymeric Nanoconstructs for Monitoring and Treating Inflammatory Bowel Disease. *Theranostics* **2017**, *7*, 3653.

(51) Di Francesco, M.; Celia, C.; Primavera, R.; D'Avanzo, N.; Locatelli, M.; Fresta, M.; Cilurzo, F.; Ventura, C. A.; Paolino, D.; Di Marzio, L. Physicochemical Characterization of Ph-Responsive and Fusogenic Self-Assembled Non-Phospholipid Vesicles for a Potential Multiple Targeting Therapy. *Int. J. Pharm.* **2017**, *528*, 18−32.

(52) Singhvi, G.; Singh, M. In-Vitro Drug Release Characterization Models. *Int. J. Pharm. Stud Res.* **2011**, *2*, 77−84.

(53) Shen, C.-M.; Mao, S. J.; Huang, G. S.; Yang, P.-C.; Chu, R.-M. Stimulation of Smooth Muscle Cell Proliferation by Ox-Ldl-and Acetyl Ldl-Induced Macrophage-Derived Foam Cells. *Life Sci.* **2001**, *70*, 443−452.

(54) Xu, S.; Huang, Y.; Xie, Y.; Lan, T.; Le, K.; Chen, J.; Chen, S.; Gao, S.; Xu, X.; Shen, X.; Huang, H.; Liu, P. Evaluation of Foam Cell Formation in Cultured Macrophages: An Improved Method with Oil Red O Staining and Dii-Oxldl Uptake. *Cytotechnology* **2010**, *62*, 473−481.

(55) Yan, P.; Xia, C.; Duan, C.; Li, S.; Mei, Z. Biological Characteristics of Foam Cell Formation in Smooth Muscle Cells Derived from Bone Marrow Stem Cells. *Int. J. Biol. Sci.* **2011**, *7*, 937.

(56) MacRitchie, N.; Grassia, G.; Sabir, S. R.; Maddaluno, M.; Welsh, P.; Sattar, N.; Ialenti, A.; Kurowska-Stolarska, M.; McInnes, I. B.; Brewer, J. M.; Garside, P.; Maffia, P. Plasmacytoid Dendritic Cells Play a Key Role in Promoting Atherosclerosis in Apolipoprotein E−Deficient Mice. *Arterioscler., Thromb., Vasc. Biol.* **2012**, *32*, 2569−2579.

(57) MacRitchie, N.; Grassia, G.; Noonan, J.; Cole, J. E; Hughes, C. E; Schroeder, J.; Benson, R. A; Cochain, C.; Zernecke, A.; Guzik, T. J; Garside, P.; Monaco, C.; Maffia, P. The Aorta Can Act as Site of Naïve Cd4+ T Cell Priming. *Cardiovasc. Res.* **2020**, *116*, 306−316.